An earthquake-triggered avalanche in Nepal in 2015 was exacerbated by climate variability and snowfall anomalies

Check for updates

Yu Zhuang[1,2] ✉, Binod Dawadi[3,4], Jakob Steiner[5,6], Rajesh Kumar Dash [7], Yves Bühler [1,2], Jessica Munch[1,2] & Perry Bartelt[1,2]

On 25 April 2015, the Gorkha earthquake triggered a large rock-ice avalanche and an air blast disaster in the Langtang Valley, Nepal. More than 350 people were killed or left missing. Here we reconstruct the evolution of the Langtang avalanche-air blast using field investigations and numerical modeling and examine the influence of two primary climate-related phenomena: snowfall anomalies and warm temperatures. Our findings suggest a deep snow cover fosters the formation of a dispersed avalanche, which increases the mobility and destructive power of the powder cloud air blast. Elevated air temperatures intensify meltwater production and lubricate the flowing mass. Both mechanisms contributed to the Langtang disaster. Our study underscores the essential impact of snow cover and air temperature on the risk assessment of high-altitude rock-ice avalanches, highlighting how seasonal and climatic variations affect avalanche runout and air blast dynamics.

Large rock-ice avalanches are geophysical mass flows composed of a mixture of rock and ice. They can be extremely hazardous due to their extremely high velocity and long runout[1–3]. In earthquake-prone regions globally changing climate appears to be exacerbating these hazards[4]. Scientists have long recognized rapid global climate change favors the instability of mountains in glacial and periglacial areas[5–7]. Nevertheless, to our knowledge, no hazard risk assessment considers how the impact of climate change contributes to their destructive potential, especially in terms of runout and flow regime transitions, such as the formation of hazardous air blasts.

One phenomenon of climate change is frequent snowfall anomalies in high-altitude regions. In the past decades, the duration of snowfall decreased, while snowfall intensity showed an increasing trend[8–10]. The thick snow cover arising from snowfall anomalies is an important mass source of the avalanche core. This snow entrainment process amplifies the avalanche volume[11,12], lubricates the avalanche movement[13], and exacerbates the formation of a rock-ice-snow powder avalanche[14]. This type of avalanche often generates powerful air blasts capable of causing damage and human fatalities far beyond the reach of avalanche core[15].

Another feature of the ongoing climate change problem is warming[16,17], moreover, how changing snow and air temperatures will change avalanche flow dynamics. In existing rock-ice avalanche models, the sliding mass is treated as a thermally insulated system, ignoring the effect of ambient environment[18,19]. Frictional shearing[20], entrainment process[13], and particle collisions[21] are heat energy sources that change the avalanche temperature and produce meltwater. It is important to note that avalanche snow (ice) exists near its melting point and frictional heating can easily supply the necessary energy input needed to produce meltwater. The porous-medium structure of avalanches and the dispersive movement of granular particles allow the intake and outburst of ambient air[14]. This interaction with the ambient environment is inevitable during avalanche movement and can either enhance or hinder the heating process. The temperature difference between the avalanche and ambient air leads to a heat exchange that greatly influences meltwater production and the flow regime of the avalanche core.

One striking example is the rock-ice avalanche of Langtang (2015), which was triggered by the Gorkha earthquake in a warm season, releasing several ice masses well above the snowline[22]. The thick snow cover amplified the avalanche volume and formed a rock-ice-snow powder avalanche. Fujita et al.[23] attributed the massive destruction caused by the avalanche directly to a snow cover anomaly. The air blast nearly destroyed the Langtang village and flattened a forest on the valley counter-slope[24].

In this paper, we reconstruct the evolution of the Langtang avalanche and generated air blasts based on documented field measurements and

[1]WSL Institute for Snow and Avalanche Research SLF, Davos Dorf, Switzerland. [2]Climate Change, Extremes and Natural Hazards in Alpine Regions Research Centre CERC, Davos Dorf, Switzerland. [3]Central Department of Hydrology and Meteorology, Tribhuvan University, Kathmandu, Nepal. [4]Kathmandu Center for Research and Education, Chinese Academy of Sciences-Tribhuvan University, Kathmandu, Nepal. [5]Himalayan University Consortium, Lalitpur, Nepal. [6]Institute of Geography and Regional Science, University of Graz, Graz, Austria. [7]Geotechnical Engineering and Geohazards (GEGH) Group, CSIR-Central Building Research Institute, Roorkee, Uttarakhand, India. ✉e-mail: yu.zhuang@slf.ch

numerical modeling. We further conduct simulations with different snow cover depths and air temperatures to investigate the impact of snow entrainment and ambient environment, indicating how seasonal and climatic influences may affect the danger of rock-ice avalanches. The study focuses exclusively on changes in runout and flow regimes under different snow cover and air temperature conditions, rather than variability in avalanche occurrence due to climate change. Our primary goal is to quantify the danger arising from rock-ice-snow avalanches, containing both a dense flow core and dust cloud, in different mountain conditions that can be eventually associated with changing climate scenarios.

Langtang avalanche

On 25 April 2015, the Gorkha earthquake (Mw7.9) triggered a large rock-ice avalanche in the Langtang Valley, Nepal. Details of the Langtang avalanche are well recorded in existing literature. Thus, here we briefly introduce the essential information concerning this disastrous event. The avalanche was initiated as a multi-source ice avalanche (initiated in several release areas) of $\sim 3.5 \times 10^6$ m^3, and the release areas are located over 6000 m a.s.l. (Fig. 1a, b). Satellite images (April–May 2015) indicated an evident snowline at 4000–4500 m a.s.l. Four anomalous snowfall events occurred during the previous winter (October 2014–April 25, 2015), resulting in a thick snow cover on the mountain surface[23]. Field investigation reveals that the released ice mass entrained snow (over 4500 m a.s.l.) and debris cover (below 4500 m a.s.l.) along the travel path (Fig. 1c)[23]. According to pre- and post-event digital surface models[25], we knew that the avalanche involved a total volume of 14.38×10^6 m^3 of rock, ice, and snow mass. Of this, a total of 6.95×10^6 m^3 accumulated in the Langtang Valley[25]. The Langtang village is located on the valley floor (Fig. 1d, e) and was not struck directly by the avalanche core. The air blast generated by the avalanche destroyed large parts of the village and caused over 350 deaths. This is confirmed by field observations showing that many houses constructed of stone slabs were flattened or destroyed by the air blast[24] (Supplementary Fig. 1a). Furthermore, the air blast impacted an area of 1 km up and down the valley and flattened a forest on the opposite mountain (Fig. 1e, Supplementary Fig. 1b), as described by Kargel et al.[22].

Two local meteorological stations record the air temperature: Kyanjing station at 3862 m a.s.l. (6.3 km away from the Langtang village) and Yala Base camp station at 5058 m a.s.l. (10.2 km from the Langtang village)[26]. The average measured temperature on 25 April was −0.65 to 9.05 °C at Kyanjing station (2012–2014, 2016–2018) and −8.10 to 0.18 °C at Yala Base camp

station (2013, 2016–2018). Another pluviometer at 4831 m a.s.l. recorded an air temperature of −0.4° to 3.6° within 30 min before the avalanche occurred, indicating a warm environment[23]. The Gorkha earthquake occurred at 11:56 Nepal Standard Time, therefore a high temperature (9 and 0 °C at 3862 and 5058 m a.s.l., arising from the recorded max value) is applied for the following analysis, indicating an air temperature gradient of ~0.75 °C per 100 m elevation difference. According to Fujita et al.[23], the snow depth at Yala station was ~1.5 m. Using this snow depth value, combined with the location of the snow line, we derived a preliminary estimate of the snow cover gradient. Based on this estimate, the snow depth at the release area was calibrated, ensuring that the entrained and total avalanche volumes match the measured data.

Results
Langtang avalanche and the generated air blast

Modeling results of the Langtang avalanche are presented in Fig. 2. The snow depth at the release area is estimated to be 3 m, and a gradient of −0.15 m per 100 m is determined with this depth value and the location of the snow line. The modeled released ice volume is 3.65×10^6 m^3, and the sliding mass entrained snow and rock materials of 11.20×10^6 m^3 during the movement process (simulated total volume of 14.85×10^6 m^3). The error between the simulated and actual volumes (initial volume of 3.50×10^6 and total volume of 14.38×10^6 m^3) is within 5%. Two main deposit areas are observed in the simulation: the platform at 4500 m a.s.l. and the Langtang Valley (Fig. 2a). The depth of deposits in the Langtang Valley is over 30 m, as observed by Fujita et al.[23]. The simulated avalanche volume and the deposit area match these observations. The calculated avalanche core reached the maximum velocity of over 90 m s^{-1} at 5000–5500 m a.s.l. When the avalanche passed the Langtang Valley, immediately before hitting the toe of the opposite mountain, it was traveling at 57 m s^{-1} (Fig. 2b), matching the velocity estimated by the run-up equation (63 m s^{-1}, Kargel et al.[22]).

Figure 2c shows the dynamic pressure of the Langtang avalanche-induced air blast. The air blast shows an impact area far beyond the avalanche core, covering the whole Langtang village and the forest on the opposite mountainside. In the Langtang village, the dynamic pressure of the air blast exceeds 15 kPa but decreases gradually to 6 kPa as it moves over the village (a rule of thumb used by avalanche engineers is that a 1 kPa air blast will violently blow a human to the ground at impact). The turbulent fluctuations greatly magnify the air blast pressure. At a specific location
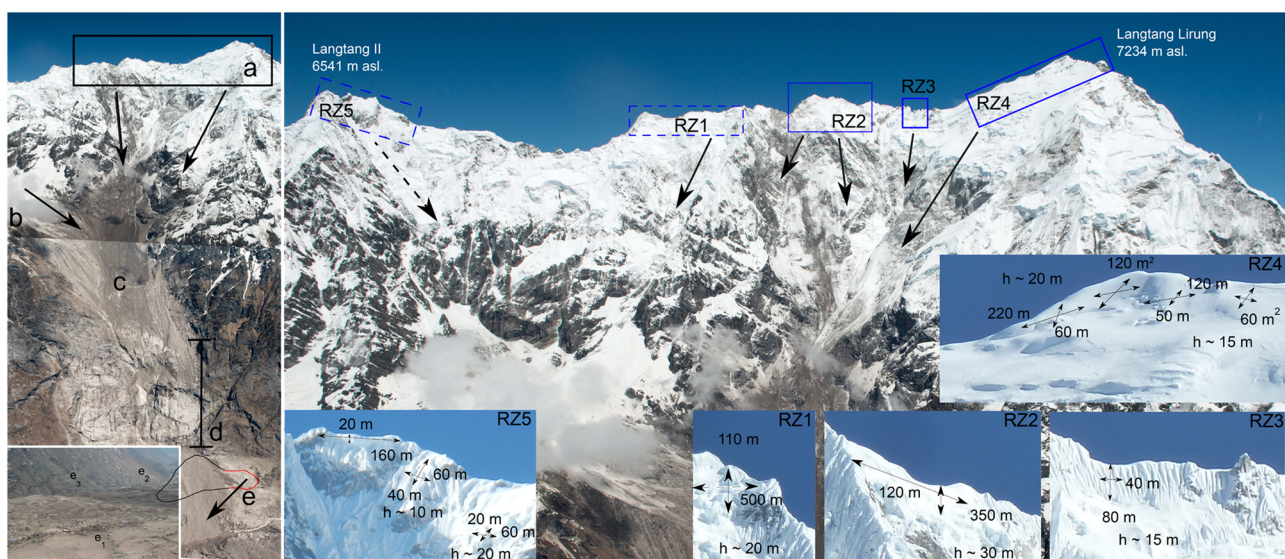

Fig. 1 | Overview of the Langtang Avalanche. a The release area from Langtang Lirung. The size of released materials helps estimate the initial volume. **b** The direction from where additional ice was released from around Langtang II. Both are shown in detail in the right part of the figure. **c** The plateau where the rock entrainment occurred. **d** The headwall above the village (height ~500 m). **e** Shows the view angle of the photo as an inset where destroyed houses (**e1**), blown-over trees (**e2**), and deposited ice–debris mix on the far side of the valley (**e3**) are shown. Images taken from the helicopter by D.F. Breashears/GlacierWorks.
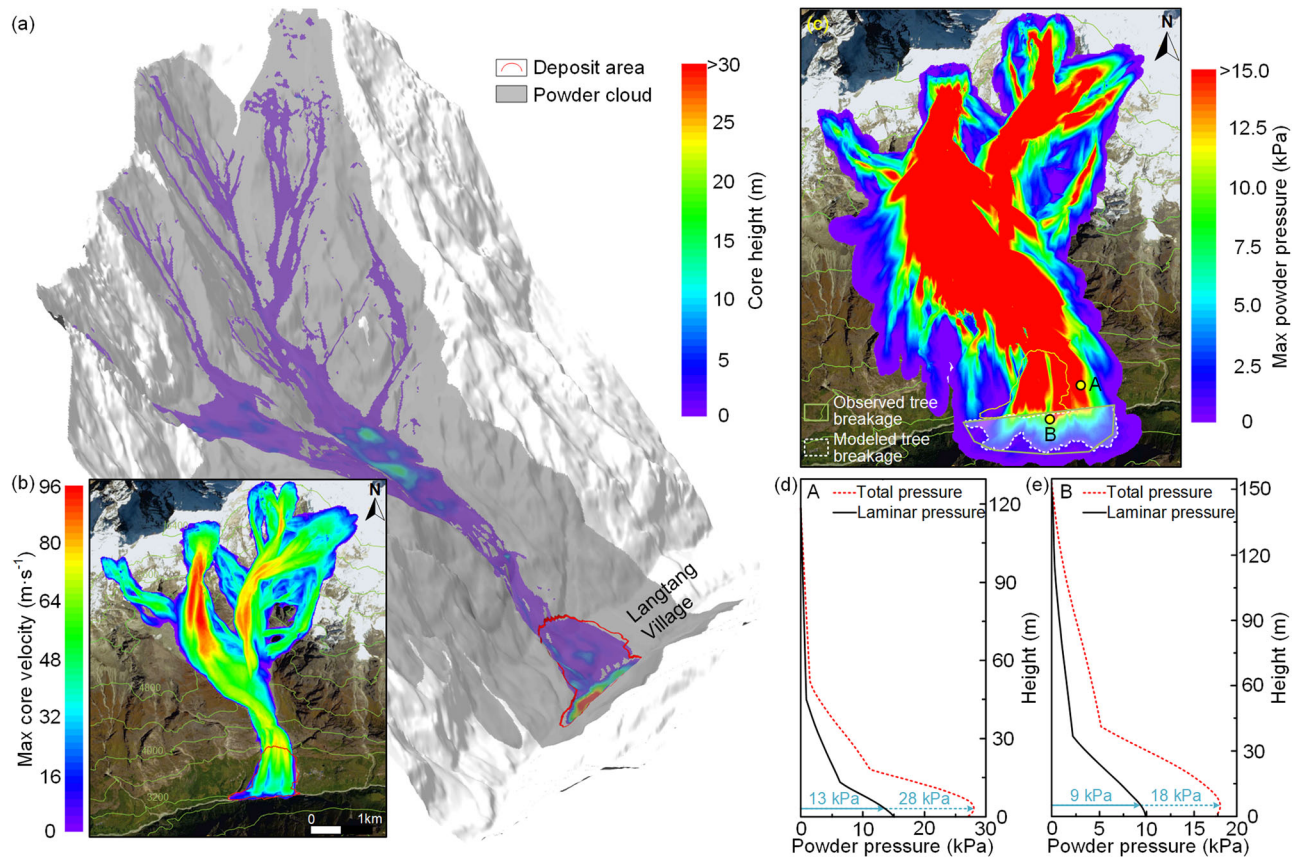
Fig. 2 | Modeling results of the Langtang avalanche and the generated air blast. a Final deposit distribution of the avalanche core, matching the observations (red lines). **b** Maximum velocity of the avalanche core. **c** Maximum mean pressure of the air blast. **d** and **e** Powder pressure profile at the Langtang village (point A in **c**) and the forest at the mountain toe (point B in **c**). The satellite image arises from Planet (Images ©2021 Planet Labs PBC).

(simulation point) near Langtang village (point A in Fig. 2c), the maximum pressure reaches 28 kPa (Fig. 2d), nearly double the pressure arising from the mean velocity. Such high pressures are capable of destroying houses, as observed. On the opposite mountain slope, the pressure of the air blast reaches a mean of 10 kPa and a maximum of 18 kPa at the mountain toe (Fig. 2e) but decreases substantially as it climbs up the mountain. Tree-breakage calculations follow the method proposed by Feistl et al.[27]. Trees on the opposite mountain face are Abies and Rhododendron species with an average diameter of 0.16 m[23]. Using a bending strength of 72 MPa, modeling results indicate a tree-breakage area of about 0.8 km², extending 1 km up and down the valley from the deposit center and 550 m up the mountain (Fig. 2c). The calculated tree-breakage area essentially matches the observations[22].

Impact of snow entrainment

We set up scenarios to investigate the impact of snow cover on the dynamics of rock-ice avalanches and air blasts. The snow cover at the release area is set at 0–3 m in depth with a constant gradient of −0.15 m per 100 m. The air temperature remains fixed. In the RAMMS model, the snow cover is adjusted based on the slope angle and curvature along with the elevation gradient to produce a realistic snow distribution on mountainous terrain. Snow cover distributions are shown in Fig. 3a–d.

Modeling results indicate a longer runout distance and higher mobility in the case of a thick snow cover (Fig. 3e–h). When the snow cover at the release area reaches 3 m, which corresponds to the modeling results in Fig. 2, the calculated avalanche dynamics match the observed conditions well. In the case without considering snow entrainment (snow cover = 0 m), the rock-ice avalanche stops before hitting the opposite mountain. The sliding mass primarily deposits at the 4500 m a.s.l. platform, with only a little mass

reaching the Langtang Valley. For the air blast hazards, the cloud dynamics are again related to the thickness of the snow cover. Both the impact area and dynamic pressure of the air blast decrease in the case of a thin snow cover (Fig. 3i–p). When there is no snow cover, the mean dynamic pressure at the Langtang village is only 2.5 kPa, and only a few trees are damaged on the opposite mountain (Fig. 3l, p), showing minor destruction compared with the actual event. This implies that the entrained snow facilitates the formation of a dispersed powder avalanche and is a primary factor that led to the Langtang disaster. Our numerical results strongly support the hypothesis of Fujita et al.[23].

Impacts of ambient temperature

Further scenarios of different air temperatures are designed to investigate the impact of temperature variation on the danger arising from rock-ice avalanches, as presented in Fig. 4. The air temperature at 3862 m a.s.l. (Kyanjing meteorological station) is set −1 to 19 °C with a constant gradient of 0.75 °C per 100 m. Here the snow cover depth remains fixed. Modeling results indicate that the avalanche core shows higher mobility in the case of a warm environment. When the air temperature at 3862 m a.s.l. reaches −1 °C, the heat transfer with the cold air restricts the melting of snow and ice. The meltwater is 74,000 t at the end of the event (Fig. 4g), and the maximum water content in the avalanche core is ~600 mm m⁻³ (Fig. 4d). In this scenario, relatively small amounts of material deposit in the Langtang Valley (Fig. 4a) compared with the actual conditions. When the air temperature is 19 °C at 3862 m a.s.l., a warm environment, the produced meltwater reaches 170,000 t (Fig. 4i), more than twice the amount calculated for a cold environment. The maximum water content in the avalanche core reaches over 1800 mm m⁻³ (Fig. 4f), a high value. The rheological relationship applied here is an ever-decreasing Coulomb friction resistance with
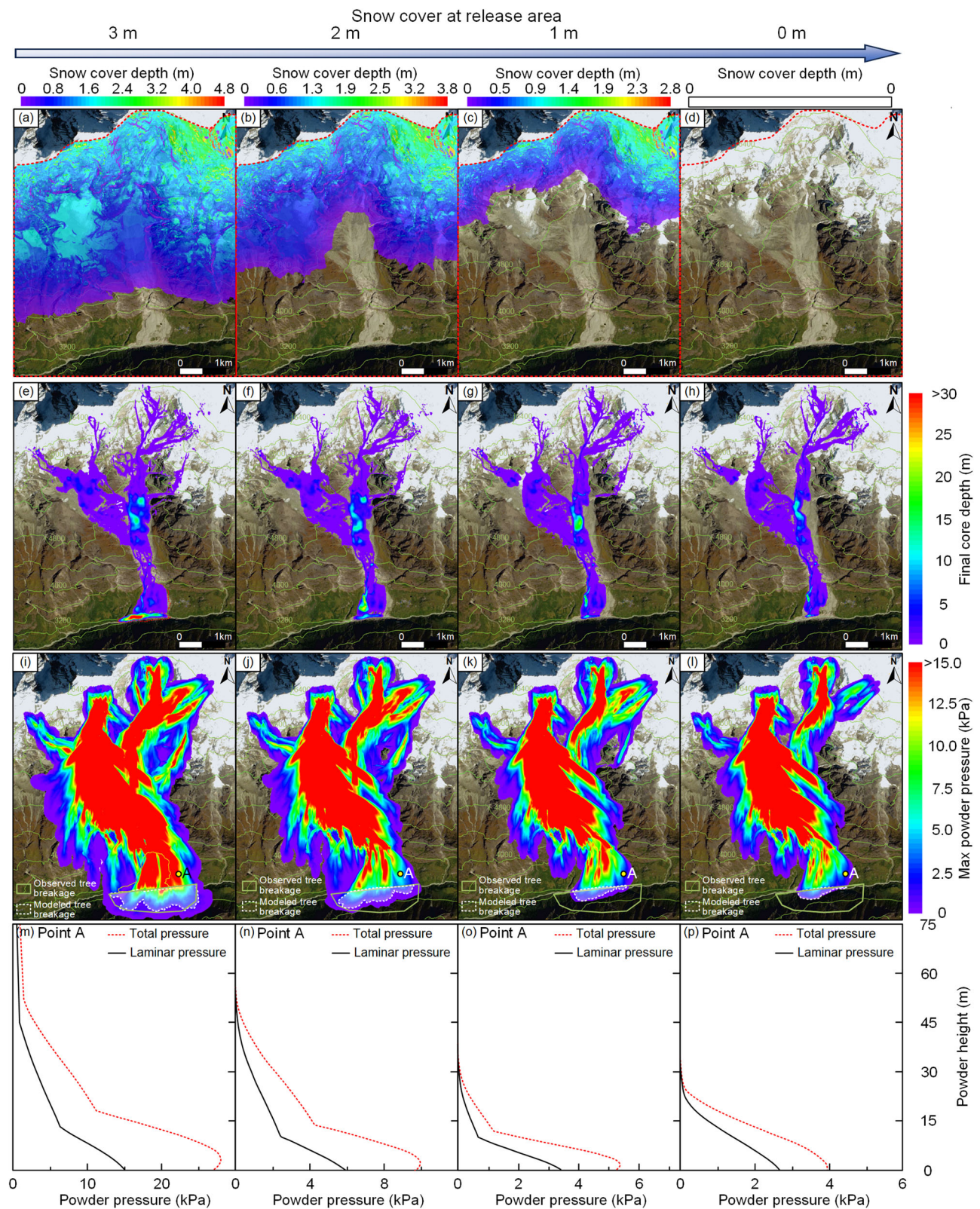
Fig. 3 | Impacts of snow entrainment on the destructive potential of the Langtang avalanche and generated air blasts. a–d Snow cover distribution in different scenarios. Red dotted line represents the calculated domain. **e–h** Impacts of snow cover on the avalanche extent. **i–l** Impacts of snow cover on the air blast dynamics. **m–p** Pressure profile at the Langtang village (Point A in **i**) in cases of different snow covers. The satellite image arises from Planet (Images ©2021 Planet Labs PBC).
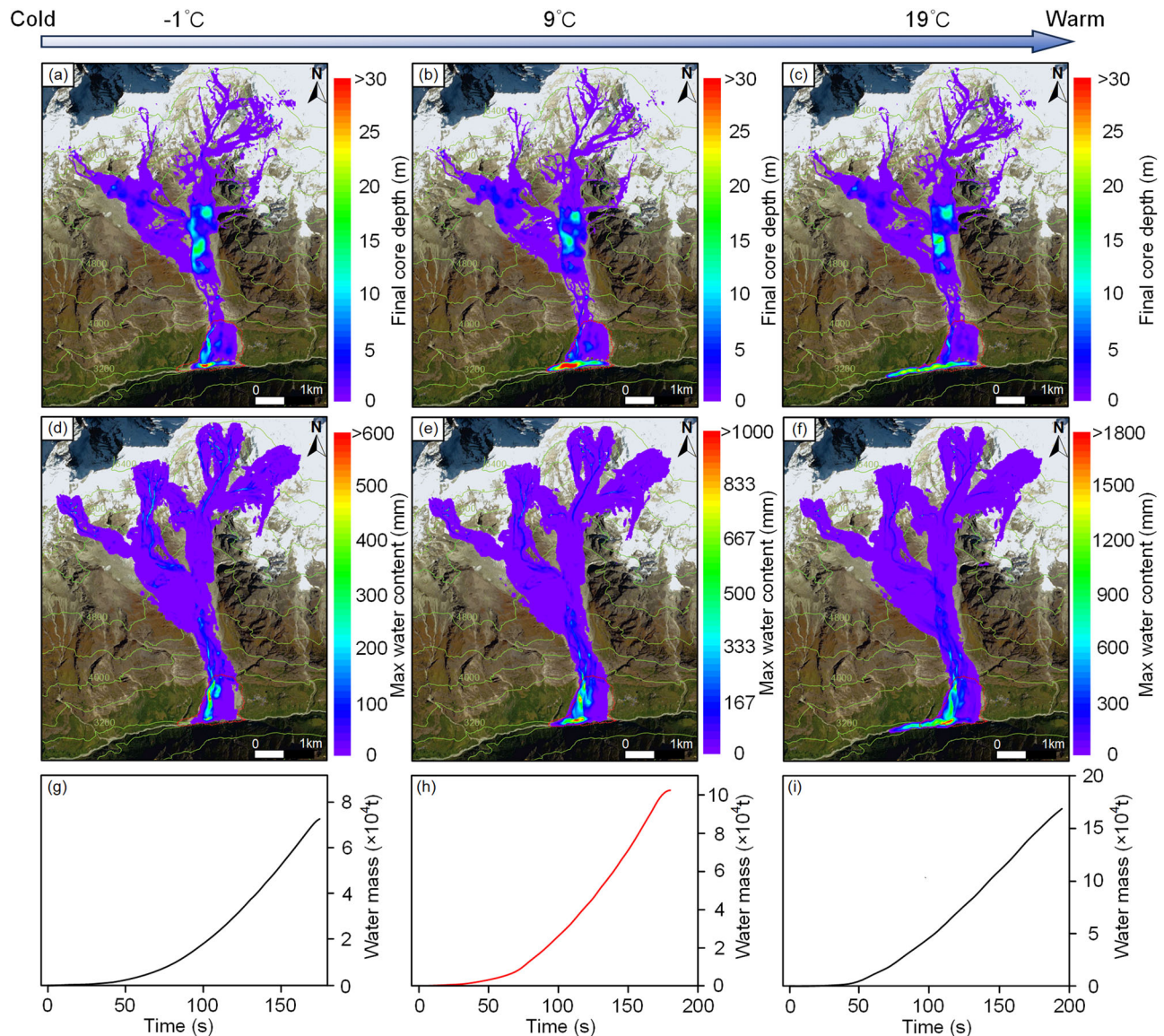
Fig. 4 | Impacts of air temperature on the avalanche extent and meltwater production. a–c Impacts of air temperature on the avalanche extent. **d–f** Impacts of air temperature on the water content distribution within the avalanche core. **g–i** Impacts of air temperature on meltwater production. Here, the air temperature is set as −1, 9, and 19 °C at 3862 m a.s.l. with a constant temperature gradient. The satellite image arises from Planet (Images ©2021 Planet Labs PBC).

increasing water content[13]:

$$\mu_w = \mu_{min} + (\mu_\Phi - \mu_{min}) \exp\left[\frac{-m_w}{m_0}\right] \qquad (1)$$

where μ_Φ is the dry friction coefficient, μ_{min} is the fully lubricated friction coefficient, representing the lowest friction, m_w is the water height in the flow and m_0 is the reference height. The friction decreases from μ_Φ (dry avalanche) to μ_{min} (fully lubricated flow) with the increase in water content. In the case of a warm environment (Fig. 4f), the abundant amount of meltwater at the avalanche front provides lubrication (decreases the friction, Supplementary Fig. 2) leading to a fluid-like flow regime in the Langtang Valley and thus a long runout distance (Fig. 4c). The avalanche moved over 1.5 km downstream of the Langtang Valley. For the Langtang avalanche, due to the low temperature of the released materials, the meltwater appears at ~20 s after the avalanche initiation and accumulates in the frontal lobe of the avalanche deposits (Fig. 4e, h).

Discussion and implications

Scientists suggest that ongoing climate change favors the initiation of rock-ice avalanches, but its impacts on avalanche formation and flow are rarely quantified[3,6,28]. With this purpose, using the Langtang avalanche, we numerically investigate two important phenomena arising from climate change to the destructive potential of rock-ice avalanches: snowfall anomalies and global warming.

Snowfall anomalies

For a rock-ice avalanche, snowfall anomalies will exacerbate the avalanche mobility and lead to an air blast problem. Anomalous snowfall and the associated thick snow cover favor snow entrainment in the mountain environment. This process can magnify the avalanche volume and change the flow behavior. Compared with ice and rock mass, snow is easily entrained because of the low shear stress threshold[29]. Snow is a material of low friction and can decrease the equivalent Coulomb frictional coefficient (in Eq. (13)) of the avalanche core. One primary consequence of the snow

entrainment is the increment of flow height, which increases the normal and shear stress acting on the ground surface. Combined with the entrainment process[12], the additional shearing work attributable to the shear stress increment exacerbates the heat energy production within the avalanche core, therefore favoring meltwater production. The lubrication effect of the meltwater greatly enhances the avalanche mobility. Furthermore, the flowing resistance is a function of fluctuation energy R_Φ (Eq. (13)), again related to the shearing work and the flow height. Chute experiments[30] indicate that friction decreases in proportion to the increase in the gravitational work rate or the shearing work rate. Without considering the entrainment process, there is no mass source for avalanches in motion. For a finite-sized avalanche, shear gradients within the avalanche core cause the flow height to decrease. The shearing work rate and production of fluctuation energy subsequently decline, and friction increases. The avalanche begins to starve and decelerate, eventually stopping on the slope.

As for the air blast hazard, the process of snow entrainment facilitates the formation of a rock–ice–snow avalanche with a dense granular core consisting of rock and ice fragments and a dust cloud of suspendable particles. The initial mass and momentum of the air blast are known to arise from the air movements caused by displacing air in the avalanche core[14]. The entrained snow is, therefore, an important mass/momentum source to transfer mass and momentum to the powder cloud, magnifying its impact area and dynamic pressure. In the case without snow entrainment, the Langtang avalanche-induced air blast hardly destroys the Langtang village and the forest (Fig. 3l), principally different from the actual conditions. This implies air blast hazards could show a higher destructive force after an intense snowfall event. We suggest the previous snowfall anomalies and the snow entrainment were a primary factor that caused the Langtang disaster.

Heat exchange with air temperature
For rock-ice avalanches, the generation of heat energy and the phase change processes are of paramount interest due to the unique properties of ice and snow[18,31]. The components of snow and ice reside close to their melting points, and the frictional heat generated during the avalanche propels these materials toward a phase transition. This process is tempered by the ambient air temperature. Recorded videos[3] and our detailed investigations into avalanche evolution provide compelling evidence of the physical interaction between the avalanche core and the ambient air temperature. The avalanche core entrains the ambient air during the movement process and outbursts the dust-mixed air to generate the powder cloud. The Reynolds number of natural rock-ice avalanches[32] reaches 10^4–10^6. Such a turbulent structure facilitates the mixture of the granular particles and entrained air, therefore exacerbating a heat exchange between the avalanche core with the ambient environment. Our modeling results of the Langtang avalanche suggest a warm air temperature amplifies the meltwater production and lubricates the flowing mass.

For simplification and engineering applications, we used an experimentally based heat transfer relationship for sphere particles[33]. Though the impacts of particle shape and porosity are ignored, this relationship is sensitive to the particle size. More precisely, the particle surface area. According to the heat transfer relationship (Eq. (12)):

$$\dot{q}_{\Phi\to\Lambda} = HA_s\left(T_\Phi - T_\Lambda\right) = \frac{\mathrm{Nu} \cdot k_a}{2r} \cdot \frac{3\rho_\Phi h_\Phi A}{4\rho_g r}\left(T_\Phi - T_\Lambda\right) = \frac{3\rho_\Phi h_\Phi A k_a}{8\rho_g} \cdot \frac{\mathrm{Nu}}{r^2} \tag{2}$$

The heat transfer is proportional to $r^{-1.5}$–$r^{-2.0}$. In this study, due to the lack of accurate particle size distribution, particle sizes for snow (7 cm), ice (10 cm), and rock (30 cm) are determined based on our practical experience with numerous historical avalanches and the existing literature[34,35]. This implies heat energy exchange between snow particles with air reaches 8.9–18.4 times rock particles of the same volume. For the Langtang avalanche, the volume of the entrained snow accounts for >70% of the total volume[23]. The process from avalanche initiation to deposition lasts ~3 min, and the air temperature in the Langtang Valley reaches ~14 °C. The small-

sized snow particles, prolonged movement, and warm air temperature intensify the heat exchange and meltwater production, resulting in a flow-like movement in the Langtang Valley. Sensitivity analysis indicates a longer runout distance, more meltwater production, and a highly fluid flow regime of avalanches in a warm environment. The impacts of heat transfer with the ambient air on meltwater production and avalanche runout can be even higher than the contribution of snowpack temperature (see extra simulations presented in Supplementary Fig. 3).

Notably, the Gorkha earthquake and Langtang avalanche occurred at noon, in a warm environment. If the avalanche occurs at night, a cold environment hinders the meltwater production and leads to a smaller runout and impact area that is similar to the scenario depicted in Fig. 4a. We are not able to predict when a catastrophic earthquake will occur, but our analysis of air temperature impacts indicates that the destructive potential of rock-ice avalanches is not only related to large-scale global warming but also to short-term diurnal temperature.

Risk assessments of rock-ice avalanches are a primary concern in high-altitude mountainous regions. Confronted with the problem of extreme and rare events and the lack of historical documentation, avalanche dynamics modeling will play a key role in assessing the safety of settlements, transportation routes, and hiking trails. To our knowledge, the impacts of climate change on the destructive potential of rock–ice avalanches are multifaceted, but rarely considered. We suggest the snowfall anomalies and warm air temperature greatly contributed to the Langtang disaster.

Conclusions
At noon on April 25, 2015, the Mw 7.9 Gorkha earthquake precipitated a large rock–ice avalanche in the Langtang Valley. The resultant air blasts obliterated the Langtang village, a nearby forest, and led to the tragic loss of over 350 lives. Through meticulous field investigations and advanced numerical modeling, we have identified two principal factors contributing to the severity of the Langtang disaster: anomalous snowfall and elevated temperatures. The substantial snow cover facilitated snow entrainment, promoting the development of a dispersed powder avalanche. This entrained snow significantly increased the avalanche volume, acted as a lubricant for the flowing mass, and amplified the destructive power of the air blast. Furthermore, the warm air temperature, in conjunction with the turbulent structure of the avalanche core, intensified heat exchange between the granular particles and the entrained air. This thermal process enhanced meltwater production, consequently altering the avalanche's mobility. These mechanisms were crucial in intensifying the Langtang disaster. We emphasize the critical finding that incorporating the effects of snow cover and air temperature factors heavily influenced by seasonal and climatic changes—is essential when performing hazard analyses for high-altitude rock-ice avalanches. Our results reveal the inherent fragility of natural systems, particularly the mobility and destructive potential of rock-ice avalanches. Minor variations in temporal factors, climatic conditions, or the antecedent state of an event can either intensify or mitigate disastrous outcomes. This insight compels us to ponder how many disasters have been averted or caused by seemingly insignificant changes in the natural environment.

Methods
Dynamic model of rock–ice avalanche
General framework. We apply a depth-averaged model to simulate the flow dynamics of the rock-ice avalanche and the generated air blast[19,36]. The avalanche core Φ and the air blast Π are described by two distinct depth-averaged layers. The core layer comprises a granular ensemble of rock, ice, and snow particles capable of dispersion and compression, changing the interstitial air space of the core. The core movement is strongly influenced by the surface terrain and allows for both air intake and outburst. During the outburst process, the avalanche core transmits mass and momentum to the cloud Π and creates a turbulent structure in the cloud[14]. The cloud is, therefore, modeled as a turbulent flow, including suspensions of ice and rock dust that are transferred from the avalanche

core. The governing equations for both the avalanche core and dust cloud are solved using well-established finite volume schemes within the software rapid mass movement simulation (RAMMS)[36].

Avalanche core Φ

Here we follow the avalanche core model[19,36]. The model involves some essential processes of an avalanche flow, including entrainment of path materials[37] and meltwater production[19]. In the model, the movement of the avalanche core Φ is described by three state valuables: the so-called co-volume height $\hat{h}_\Phi$, the dispersed or flowing height h_Φ and the depth-averaged velocity $\vec{u}_\Phi$ that parallel to the slope surface. The co-volume represents the densest packing of ice/rock granules found in the deposit area, corresponding to a co-volume density $\hat{\rho}_\Phi$. Because the avalanche core is a multiphase flow of mixed components, the co-volume height $\hat{h}_\Phi$ is defined as

$$\hat{h}_\Phi = \frac{\rho_i}{\hat{\rho}_\Phi}\hat{h}_i + \frac{\rho_s}{\hat{\rho}_\Phi}\hat{h}_s + \frac{\rho_r}{\hat{\rho}_\Phi}\hat{h}_r + \frac{\rho_w}{\hat{\rho}_\Phi}\hat{h}_w \tag{3}$$

where ρ_i, ρ_s, ρ_r, ρ_w, $\hat{h}_i$, $\hat{h}_s$, $\hat{h}_r$, $\hat{h}_w$ are the material density and co-volume height of ice, snow, rock, and water, respectively. The model assumes both constant density and velocity profiles of each material. The primary governing equations are as follows:

$$\left(\hat{h}_\Phi\right)_t + div\left(\hat{h}_\Phi\vec{u}_\Phi\right) = \frac{\rho_\Sigma}{\hat{\rho}_\Phi}\dot{M}_{\Sigma\to\Phi} - \frac{\hat{\rho}_\Pi}{\hat{\rho}_\Phi}\dot{M}_{\Phi\to\Pi} \tag{4}$$

$$\left(h_\Phi\right)_t + \mathrm{div}\left(h_\Phi\vec{u}_\Phi\right) = \mathbb{D}\left(t, k_z, \dot{k}_z, \ddot{k}_z\right) \tag{5}$$

$$\begin{cases} \left(\hat{h}_r\right)_t + div\left(\hat{h}_r\vec{u}_\Phi\right) = \frac{\rho_\Sigma}{\rho_r}\eta_r\dot{M}_{\Sigma\to\Phi} - \nu_r\dot{M}_{\Phi\to\Pi r} \\[6pt] \left(\hat{h}_i\right)_t + div\left(\hat{h}_i\vec{u}_\Phi\right) = \frac{\rho_\Sigma}{\rho_i}\eta_i\dot{M}_{\Sigma\to\Phi} - \frac{\dot{Q}_m}{\rho_i L} - \frac{\theta_i}{\theta_i+\theta_s}\nu_i\dot{M}_{\Phi\to\Pi i} \\[6pt] \left(\hat{h}_s\right)_t + div\left(\hat{h}_s\vec{u}_\Phi\right) = \frac{\rho_\Sigma}{\rho_s}\eta_s\dot{M}_{\Sigma\to\Phi} - \frac{\dot{Q}_m}{\rho_s L} - \frac{\theta_s}{\theta_i+\theta_s}\frac{\rho_i}{\rho_s}\nu_i\dot{M}_{\Phi\to\Pi i} \\[6pt] \left(\hat{h}_w\right)_t + div\left(\hat{h}_w\vec{u}_\Phi\right) = \frac{\rho_\Sigma}{\rho_w}\eta_w\dot{M}_{\Sigma\to\Phi} + \frac{\dot{Q}_m}{\rho_w L} \end{cases} \tag{6}$$

$$\left(\hat{h}_\Phi\vec{u}_\Phi\right)_t + div\left(\hat{h}_\Phi\vec{u}_\Phi\bigotimes\vec{u}_\Phi + p_\Phi I\right) = \vec{G}\hat{h}_\Phi - \frac{\vec{u}_\Phi}{||\vec{u}_\Phi||}S_\Phi - \frac{\hat{\rho}_\Pi}{\hat{\rho}_\Phi}\dot{M}_{\Phi\to\Pi}\vec{u}_\Phi \tag{7}$$

$$\left(\hat{h}_\Phi R_\Phi\right)_t + \mathrm{div}\left(R_\Phi\hat{h}_\Phi\vec{u}_\Phi\right) = \alpha_\Phi\dot{W}_\Phi - \dot{M}_{\Phi\to\Pi}R_\Phi - \beta_\Phi\hat{h}_\Phi R_\Phi \tag{8}$$

$$\begin{aligned} \left(\hat{h}_\Phi E_\Phi\right)_t + \mathrm{div}\left(E_\Phi\hat{h}_\Phi\vec{u}_\Phi\right) &= \left[1-\alpha_\Phi\right]\dot{W}_\Phi \\ &+ \beta_\Phi\hat{h}_\Phi R_\Phi + \rho_\Sigma\left[c_\Sigma T_\Sigma + \frac{1}{2}||\vec{u}_\Phi||^2\right]\dot{M}_{\Sigma\to\Phi} - \dot{Q}_m - \dot{q}_{\Phi\to\Lambda} \end{aligned} \tag{9}$$

$$\left(m_\Phi\right)_t + \mathrm{div}\left(m_\Phi\vec{u}_\Phi\right) = \frac{\dot{Q}_m}{[\rho_w L]} \tag{10}$$

$$\int_0^{\Delta t}\dot{Q}_m dt = \rho_w c_\Phi h_\Phi\left[T_\Phi - T_m\right] \tag{11}$$

Equations (4) and (7) represent the mass and momentum balances of the avalanche core, which involves the avalanche entrainment $\dot{M}_{\Sigma\to\Phi}$ and mass/momentum transfer to the cloud $\dot{M}_{\Phi\to\Pi}$. Equation (5) describes the dispersive movement of the avalanche core. The term $\mathbb{D}(t, k_z, \dot{k}_z, \ddot{k}_z)$ represents the variation of core height due to dispersive pressure effects; we employ the model presented in Buser and Bartelt[38]. Equation (6) is the mass balance of each phase in the core, including rock, ice, snow, and water. The mass change of each phase arises from the entrainment process, air blast initiation, and phase change. Equations (8) and (9) show the balance of

fluctuation energy and heat energy. Equation (10) describes the production and transport of meltwater in the avalanche core. The meltwater arises from both the ice melting and snow melting. The model assumes the mean core temperature T_Φ never exceeds the melting temperature of T_m until all the ice and snow melt. The heat energy applied for meltwater production is presented in Eq. (11). The parameters included in Eqs. (4)–(11) are well described by Bartelt et al.[19] and Munch et al.[39] and are listed in Table 1.

In the heat energy balance of Eq. (9), the heat transfer from avalanche to the ambient, entrained air is newly involved, defined as

$$\dot{q}_{\Phi\to\Lambda} = HA_s(T_\Phi - T_\Lambda) \tag{12}$$

where $A_s = n\pi r^2$, $n = \frac{3\rho_\Phi h_\Phi A}{4\rho_g\pi r^3}$ is the particle number, ρ_g is the particle density, r is the particle radius, $T_\Phi - T_\Lambda$ represents the temperature difference between the avalanche core T_Φ and the ambient air T_Λ. $H = \frac{Nu\cdot k_a}{2r}$ is the experimentally based heat transfer coefficient[33], $k_a = 0.0257$ W m^{-1} K^{-1} is the thermal conductivity, $Nu = 2 + 0.6\mathrm{Re}^{\frac{1}{2}}\mathrm{Pr}^{\frac{1}{3}}$ is the dimensionless Nusselt number, $Re = \frac{2ur}{\nu_a}$ is the Reynolds number, $Pr = \frac{c_a\nu_a}{k_a}$ is the Prandtl number of the air, c_a is the specific heat capacity of the air.

A fundamental feature of the avalanche core model is the partitioning of a primary dissipative process, shearing, into the production of heat E_Φ (internal energy) and non-directional kinetic energy R_Φ (granular temperature). The work done by shearing $\dot{W}_\Phi = S_\Phi||\vec{u}_\Phi||$ is divided into microscopic and macroscopic random energy (heat and granular fluctuations) by parameter α_Φ [38]. Shearing is controlled by the process-based Voellmy-type rheology[40]:

$$S_\Phi = \mu_\Phi(R_\Phi, T_\Phi, m_w)\rho_\Phi gh\cos\theta + \rho_\Phi g\frac{u_\Phi^2}{\xi_\Phi(R_\Phi, T_\Phi, m_w)} \tag{13}$$

where (μ_Φ, ξ_Φ) are the Coulomb and turbulent friction coefficients, respectively, defined as functions of the fluctuation energy R_Φ, temperature T_Φ and water content m_w. The flow friction S_Φ is dependent on the dispersive properties of the random energy R_Φ, avalanche mobility, and, therefore, the formation of the powder cloud is strongly influenced by the shearing process.

Powder cloud Π

A similar set of partial differential equations is proposed to describe the movement of the powder cloud Π. To track the mass changes of different materials in the cloud, an improvement of the model is to suggest the powder cloud as a mixture of a rock powder cloud Π_r and an ice powder cloud Π_i. Therefore, the cloud density depends on the volumetric ratio of rock and ice within the cloud. We begin by presenting the mass balance equations:

$$\left(\hat{h}_{\Pi r}\right)_t + \mathrm{div}\left(\hat{h}_{\Pi r}\vec{u}_\Phi\right) = \dot{M}_{\Phi\to\Pi r} \tag{14}$$

$$\left(\hat{h}_{\Pi i}\right)_t + \mathrm{div}\left(\hat{h}_{\Pi i}\vec{u}_\Phi\right) = \dot{M}_{\Phi\to\Pi i} \tag{15}$$

$$\left(\hat{h}_\Pi\right)_t + \mathrm{div}\left(\hat{h}_\Pi\vec{u}_\Phi\right) = \frac{\hat{\rho}_{\Pi r}}{\hat{\rho}_\Pi}\dot{M}_{\Phi\to\Pi r} + \frac{\hat{\rho}_{\Pi i}}{\hat{\rho}_\Pi}\dot{M}_{\Phi\to\Pi i} \tag{16}$$

$$\left(h_\Pi\right)_t + \mathrm{div}\left(h_\Pi\vec{u}_\Pi\right) = \frac{\rho_r - \hat{\rho}_{\Pi r}}{\rho_r - \rho_\Lambda}\dot{M}_{\Phi\to\Pi r} + \frac{\rho_i - \hat{\rho}_{\Pi i}}{\rho_i - \rho_\Lambda}\dot{M}_{\Phi\to\Pi i} + \dot{M}_{\Lambda\to\Pi} \tag{17}$$

Equations (14) and (15) represent the mass balance of the rock powder cloud Π_r and ice powder cloud Π_i, respectively, and Eq. (16) described the mass balance of the total powder cloud Π. Similar to the core, $(\hat{h}_{\Pi r}, \hat{h}_{\Pi i}, \hat{h}_\Pi)$ represents the initial height of Π_r, Π_i and Π, respectively, and are given by

Table 1 | Description of variables in the rock–ice avalanche-air blast model

Symbol	Description
$\hat{h}_\Phi, \hat{h}_\Pi$	Co-volume height of the avalanche core and the total powder cloud
$\hat{\rho}_\Phi, \hat{\rho}_\Pi$	Co-volume density of avalanche core and the total powder cloud
$\hat{h}_i, \hat{h}_s, \hat{h}_r, \hat{h}_w$	Co-volume height of ice, snow, rock, and water within the avalanche core
$\hat{h}_{\Pi r}, \hat{h}_{\Pi i}$	Co-volume height of the rock powder cloud and ice powder cloud
$\hat{\rho}_{\Pi r}, \hat{\rho}_{\Pi i}$	Co-volume density of the rock powder cloud and ice powder cloud
$\rho_i, \rho_s, \rho_r, \rho_w$	Density of ice, snow, rock, and water
h_Φ, h_Π	Flowing height of core and true height of cloud
$\rho_\Phi, \rho_\Pi, \rho_\Sigma, \rho_\Lambda$	Flowing core density, true cloud density, entrainment density, and air density
$\vec{u}_\Phi, \vec{u}_\Pi$	Mean slope parallel velocities of core and cloud
$\vec{u}\prime_\Pi$	Velocity fluctuation of cloud
$\dot{M}_{\Sigma\to\Phi}$	Rate of path entrainment in avalanche core
$\dot{M}_{\Phi\to\Pi},$ $\dot{M}_{\Phi\to\Pi r}, \dot{M}_{\Phi\to\Pi i}$	Core mass injected into the total, rock and ice powder cloud
$\dot{M}_{\Lambda\to\Pi}$	Air entrainment into the powder cloud
$\dot{Q}_m$	Rate of heat energy loss for ice melting
$\dot{q}_{\Phi\to\Lambda}$	Heat transfer between core and the ambient environment
$R_\Phi, R_\Pi, \beta_\Phi, \beta_\Pi$	Fluctuation energy of core and cloud, β_Φ and β_Π control the decay of fluctuation energy
$\alpha_L, \alpha_T, \mu_L, \mu_T$	Laminar/turbulent parameters controlling air entrainment and drag resistance
S_Φ, S_Π	Core and cloud friction
$\dot{W}_\Phi, \dot{W}_\Pi$	Shearing work of core and cloud
$k_z, \dot{k}_z, \ddot{k}_z$	Location, velocity, and acceleration of the centroid of the core perpendicular to the slope
$\vec{G}$	Gravitational acceleration
$T_\Phi, T_\Sigma, T_m, T_\Lambda$	Temperature of core, entrained material, water, and ambient environment
L	Latent heat
c_Σ, c_Φ	Specific heat capacity of entrainment and core
m_Φ	Mass of water
E_Φ	Heat energy of the core
α_Φ	Splitting factor to separate the shearing work within the core
ν_r, ν_i	Volumetric fraction of rock-dust and ice-dust in the initial cloud
θ_i, θ_s	Volumetric fraction of ice and snow in the core
$\eta_r, \eta_i, \eta_s, \eta_w,$	Mass fraction of rock, ice, snow, and water in the entrained material

the initial cloud density ($\hat{\rho}_{\Pi r}$, $\hat{\rho}_{\Pi i}$ and $\hat{\rho}_\Pi$) before blowing out from the avalanche core Φ. The true cloud height h_Π is affected by clouds ejected from the core ($\dot{M}_{\Phi\to\Pi r}, \dot{M}_{\Phi\to\Pi i}$) and ambient air entrainment $\dot{M}_{\Lambda\to\Pi}$. Due to this air entrainment, the cloud height increases during the propagation process and the density decreases to ρ_Π, satisfying $\rho_\Pi = \rho_i \frac{\nu_i \hat{h}_{\Pi i}}{h_\Pi + \nu_i \hat{h}_{\Pi i} + \nu_r \hat{h}_{\Pi r}} + \rho_r \frac{\nu_r \hat{h}_{\Pi r}}{h_\Pi + \nu_i \hat{h}_{\Pi i} + \nu_r \hat{h}_{\Pi r}} + \rho_\Lambda \frac{h_\Pi}{h_\Pi + \nu_i \hat{h}_{\Pi i} + \nu_r \hat{h}_{\Pi r}}$, $\rho_i = 971$ kg m^{-3} is the ice density, $\rho_r = 2500$ kg m^{-3} is the rock density, $\rho_\Lambda = 1.225$ kg m^{-3} is the air density ($\nu_i = \frac{\hat{\rho}_{\Pi i} - \rho_\Lambda}{\rho_i - \rho_\Lambda}$, $\nu_r = \frac{\hat{\rho}_{\Pi r} - \rho_\Lambda}{\rho_r - \rho_\Lambda}$) represents the solid fraction in the initial ice and rock powder cloud.

The momentum balance of the powder cloud is

$$\left(\hat{h}_\Pi \vec{u}_\Pi\right)_t + \text{div}\left(\hat{h}_\Pi \vec{u}_\Pi \bigotimes \vec{u}_\Pi + p_\Pi I\right) = \dot{M}_{\Phi\to\Pi} \vec{u}_\Phi + \frac{(\hat{\rho}_\Pi - \rho_\Lambda)}{\hat{\rho}_\Pi} \vec{G} \hat{h}_\Pi - \frac{\vec{u}_\Pi}{||\vec{u}_\Pi||} S_\Pi \tag{18}$$

The mixed ice/rock powder cloud moves with a mean velocity vector $\vec{u}_\Pi$. The cloud is driven by the initial momentum transferred from the avalanche core $\dot{M}_{\Phi\to\Pi} \vec{u}_\Phi$ and the gravity $\frac{(\rho_\Pi - \rho_\Lambda)}{\rho_\Pi} \vec{G}$.

Another important improvement of the proposed model is the inclusion of turbulence. The instantaneous air blast velocity $\widetilde{u}_\Pi$ is written as the sum of a mean $\vec{u}_\Pi$ and a fluctuating component $\vec{u}\prime_\Pi$. The energy associated with the fluctuation of the granules $R_\Pi(x, y, z, t)$ can be written as[41]

$$R_\Pi(x, y, z, t) = \frac{\hat{\rho}_\Pi}{2}\left[u_x\prime^2(t) + u_y\prime^2(t) + u_z\prime^2(t)\right] = \frac{\hat{\rho}_\Pi}{2} u\prime^2_\Pi(t) \tag{19}$$

The fluctuation energy is divided into three orthogonal components in the x, y, z directions. Here the velocity fluctuation is assumed to be isotropic, and thus $R_{\Pi,x} = R_{\Pi,y} = R_{\Pi,z} = \frac{1}{3} R_\Pi$. The balance equation of the fluctuation energy can be written as:

$$\left(\hat{h}_\Pi R_\Pi\right)_t + \text{div}\left(R_\Pi \hat{h}_\Pi \vec{u}_\Pi\right) = \dot{M}_{\Phi\to\Pi} R_\Phi + \dot{W}_\Pi + \frac{1}{2}\rho_\Lambda \dot{M}_{\Lambda\to\Pi} u^2_\Pi - \beta_\Pi \hat{h}_\Pi R_\Pi \tag{20}$$

We suggest the fluctuation energy has three sources: fluctuation energy that is created in the avalanche core and transported to the cloud $\dot{M}_{\Phi\to\Pi} R_\Phi$, internal shearing $\dot{W}_\Pi = \left[S_\Pi\right]||\vec{u}_\Pi||$ and air entrainment $\frac{1}{2}\rho_\Lambda \dot{M}_{\Lambda\to\Pi} u^2_\Pi$. The fluctuation energy R_Π of the cloud has a short lifetime and its dissipation is controlled by a decay coefficient β_Π [15].

In the air blast model, the air entrainment $\dot{M}_{\Lambda\to\Pi}$ and drag resistance S_Π are defined as a contribution of both laminar and turbulent parts. Air entrainment is suggested as a function of the turbulent velocity[42,43], the square root of the turbulent energy R_Π: $\dot{M}_{\Lambda\to\Pi} = \alpha_L(\rho_\Pi - \rho_\Lambda) + \alpha_T\sqrt{R_\Pi \hat{h}_\Pi}(\rho_\Pi - \rho_\Lambda)$. The drag resistance is suggested as a direct function of the average velocity and turbulent energy: $S_\Pi = \rho_\Pi(\mu_L u_\Pi + \mu_T R_\Pi \hat{h}_\Pi)$. The parameters ($\alpha_L, \alpha_T$) and ($\mu_L, \mu_T$) are sets of laminar/turbulent parameters controlling air entrainment and drag resistance. These parameters, along with the turbulent decay parameter β_Π control the magnitude of the avalanche air blast.

The vertical profiles of the velocity, density, and dynamic pressure, which are greatly influential to assess the air blast hazard, refer to Zhuang et al.[15]. The velocity profile follows a parabolic form and is determined using the boundary turbulent velocity values and the mean value. The density profile follows a linear profile decreasing from the bottom to the top of the cloud. Therefore, the vertical profile of the total pressure is written as $P(z) = \frac{1}{2} \cdot \rho_\Pi(z) \cdot u_\Pi(z)^2 = \frac{1}{2} \cdot \rho_\Pi(z) \cdot [\bar{u}_\Pi(z) + u\prime_\Pi(z)]^2$. Here, we assume the worst case is that the fluctuation velocity is always in the same direction as the laminar mean velocity. In this study, we applied DEM arising from SPOT satellite images to do the simulation, referring to Ragettli et al.[44].

Tree-breakage calculation

The assessment of air blast-induced tree breakage follows the method proposed by Feistl et al.[27]. The tree bending stress arising from the air blast loading is

$$\sigma_\Pi = c_\Pi \rho_\Pi \frac{8\widetilde{u}^2_\Pi}{\pi d^3} wH^2 \cos\gamma \tag{21}$$

where c_Π is the drag coefficient, $\widetilde{u}_\Pi$ is the instantaneous air blast velocity, which is the sum of the mean velocity $\vec{u}_\Pi$ and turbulent velocity $u\prime$, ρ_Π is the cloud density, (w, H, d) represents the stem diameter, height and effective

crown width of trees, respectively, γ is slope angle. The tree breakage occurs when the bending stress σ_Π exceeds the experienced tree strength.

Data availability

Code availability

The RAMMS::RockIce model used in this study is available at https://ramms.ch/.

References

1. Huggel, C., Caplan-Auerbach, J., Waythomas, C. F. & Wessels, R. L. Monitoring and modeling ice-rock avalanches from ice-capped volcanoes: a case study of frequent large avalanches on Iliamna Volcano, Alaska. *J. Volcanol. Geotherm. Res.* **168**, 114–136 (2007).
2. Schneider, D. et al. Insights into rock-ice avalanche dynamics by combined analysis of seismic recordings and a numerical avalanche model. *J. Geophys. Res.: Earth Surf.* **115**, F04026 (2010).
3. Shugar, D. H. et al. A massive rock and ice avalanche caused the 2021 disaster at Chamoli, Indian Himalaya. *Science* **373**, 300–306 (2021).
4. Gruber, S. et al. Review article: Inferring permafrost and permafrost thaw in the mountains of the Hindu Kush Himalaya region. *Cryosphere* **11**, 81–99 (2017).
5. Ballesteros-Cánovas, J. A., Trappmann, D., Madrigal-González, J., Eckert, N. & Stoffel, M. Climate warming enhances snow avalanche risk in the Western Himalayas. *Proc. Natl Acad. Sci. USA* **115**, 3410–3415 (2018).
6. Kääb, A. et al. Massive collapse of two glaciers in western Tibet in 2016 after surge-like instability. *Nat. Geosci.* **11**, 114–120 (2018).
7. Fan, X. M. et al. Imminent threat of rock-ice avalanches in High Mountain Asia. *Sci. Total Environ.* **836**, 155380 (2022).
8. Bai, L. et al. Change in the spatiotemporal pattern of snowfall during the cold season under climate change in a snow-dominated region of China. *Int. J. Climatol.* **39**, 5702–2719 (2019).
9. Lin, W. & Chen, H. Changes in the spatial–temporal characteristics of daily snowfall events over the Eurasian continent from 1980 to 2019. *Int. J. Climatol.* **42**, 1841–1853 (2022).
10. Marshall, A. M., Link, T. E., Robinson, A. P. & Abatzoglou, J. T. Higher snowfall intensity is associated with reduced impacts of warming upon winter snow ablation. *Geophys. Res. Lett.* **47**, e2019GL086409 (2020).
11. Sovilla, B., Burlando, P. & Bartelt, P. Field experiments and numerical modeling of mass entrainment in snow avalanches. *J. Geophys. Res.: Earth Surf.* **111**, F03007 (2006).
12. Vera Valero, C., Wikstroemjones, K., Bühler, Y. & Bartelt, P. Release temperature, snow-cover entrainment and the thermal flow regime of snow avalanches. *J. Glaciol.* **61**, 173–184 (2015).
13. Vera Valero, C., Wever, N., Christen, M. & Bartelt, P. Modeling the influence of snow cover temperature and water content on wet-snow avalanche runout. *Nat. Hazards Earth Syst. Sci.* **18**, 869–887 (2018).
14. Bartelt, P., Buser, O., Vera Valero, C. & Bühler, Y. Configurational energy and the formation of mixed flowing powder snow and ice avalanches. *Ann. Glaciol.* **57**, 179–188 (2016).
15. Zhuang, Y. et al. Tree blow-down by snow avalanche air blasts: dynamic magnification effects and turbulence. *Geophys. Res. Lett.* **50**, e2023GL105334 (2023).
16. Vinnikov, K. Y. & Grody, N. C. Global warming trend of mean tropospheric temperature observed by satellites. *Science* **302**, 269–272 (2003).
17. Hansen, J. et al. Global temperature change. *Proc. Natl Acad. Sci. USA* **103**, 14288–14293 (2006).
18. Pudasaini, S. P. & Krautblatter, M. A two-phase mechanical model for rock-ice avalanches. *J. Geophys. Res.: Earth Surf.* **119**, 2272–2290 (2014).
19. Bartelt, P., Christen, M., Bühler, Y. & Buser, O. Thermomechanical modelling of rock avalanches with debris, ice and snow entrainment. *Numer. Methods Geotech. Eng. IX.* **2**, 1047–1054 (2018).
20. Pudasaini, S. P., & Hutter, K. *Avalanche Dynamics: Dynamics of Rapid Flows of Dense Granular Avalanches* (Springer-Verlag, Berlin, 2007).
21. Kisuka, F., Hare, C. & Wu, C. Y. Heat generation during oblique particle impact. *Powder Technol.* **422**, 118481 (2023).
22. Kargel, J. S. et al. Geomorphic and geologic controls of geohazards induced by Nepal's 2015 Gorkha earthquake. *Science* **351**, aac8353 (2016).
23. Fujita, K. et al. Anomalous winter-snow-amplified earthquake-induced disaster of the 2015 Langtang avalanche in Nepal. *Nat. Hazards Earth Syst. Sci.* **17**, 749–764 (2017).
24. Zhuang, Y., Xu, Q., Xing, A., Bilal, M. & Gnyawali, K. R. Catastrophic air blasts triggered by large ice/rock avalanches. *Landslides* **20**, 53–64 (2023).
25. Lacroix, P. Landslides triggered by the Gorkha earthquake in the Langtang valley, volumes and initiation processes. *Earth Planets Space* **68**, 1–10 (2016).
26. Steiner, J. F. et al. Multi-year observations of the high mountain water cycle in the Langtang catchment, Central Himalaya. *Hydrol. Process.* **35**, e14189 (2021).
27. Feistl, T. et al. Forest damage and snow avalanche flow regime. *Nat. Hazards Earth Syst. Sci.* **15**, 1275–1288 (2015).
28. Yang, Q., Su, Z., Cheng, Q., Ren, Y. & Cai, F. High mobility of rock-ice avalanches: insights from small flume tests of gravel–ice mixtures. *Eng. Geol.* **260**, 105260 (2019).
29. Föhn, P. M. B., Camponovo, C. & Krüsi, G. Mechanical and structural properties of weak snow layers measured in situ. *Ann. Glaciol.* **26**, 1–6 (1998).
30. Bartelt, P., Buser, O. & Platzer, K. Starving avalanches: frictional mechanisms at the tails of finite-sized mass movements. *Geophys. Res. Lett.* **34**, L20407 (2007).
31. Sansone, S., Zugliani, D. & Rosatti, G. A mathematical framework for modelling rock-ice avalanches. *J. Fluid Mech.* **919**, A8 (2021).
32. Dong, Z. B. & Su, L. J. Flow regimes and basal normal stresses in rock–ice avalanches by experimental rotating drum tests. *Cold Reg. Sci. Technol.* **218**, 104081 (2024).
33. Ranz, W. & Marshall, W. Evaporation from drops. *Chem. Eng. Prog.* **48**, 141–146 (1952).
34. Bartelt, P. & McArdell, B. W. Granulometric investigations of snow avalanches. *J. Glaciol.* **55**, 829–833 (2009).
35. Gnyawali, K. R., Xing, A. G. & Zhuang, Y. Dynamic analysis of the multistaged ice-rock debris avalanche in the Langtang valley triggered by the 2015 Gorkha earthquake, Nepal. *Eng. Geol.* **265**, 105440 (2020).
36. Christen, M., Kowalski, J. & Bartelt, P. Numerical simulation of dense snow avalanches in three-dimensional terrain. *Cold Reg. Sci. Technol.* **63**, 1–14 (2010).
37. Frank, F. et al. Debris-flow modeling at Meretschibach and Bondasca catchments, Switzerland: sensitivity testing of field-data-based entrainment model. *Nat. Hazards Earth Syst. Sci.* **17**, 801–815 (2017).
38. Buser, O. & Bartelt, P. Production and decay of random kinetic energy in granular snow avalanches. *J. Glaciol.* **55**, 3–12 (2009).
39. Munch, J., Bartelt, P. & Christen, M. Multi-component avalanches for rock-and ice-falls to potential debris flow transition modelling. *E3S Web Conf.* **415**, 01017 (2023).
40. Salm, B. Flow, flow transition and runout distances of flowing avalanche. *Ann. Glaciol.* **18**, 221–226 (1993).
41. Richard, G. L. & Gavrilyuk, S. L. A new model of roll waves: comparison with Brock's experiments. *J. Fluid Mech.* **698**, 374–405 (2012).

42. Vallet, J., Turnbull, B., Joly, S. & Dufour, F. Observations on powder snow avalanches using videogrammetry. *Cold Reg. Sci. Technol.* **39**, 153–159 (2004).
43. Turnbull, B. & McElwaine, J. N. A comparison of powder-snow avalanches at Valle´e de la Sionne, Switzerland, with plume theories. *J. Glaciol.* **53**, 30–40 (2007).
44. Ragettli, S., Bolch, T. & Pellicciotti, F. Heterogeneous glacier thinning patterns over the last 40 years in Langtang Himal, Nepal. *Cryosphere* **10**, 2075–2097 (2016).

Author contributions
Yu Zhuang designed the work, built the model, did the simulation, analyzed the results, and wrote the manuscript. Binod Dawadi, Rajesh Dash, and Yves Bühler did the field investigation and helped analyze the results. Jakob Steiner contributed to the paper revision and provided the release volume estimates, air temperature information, and DEM. Yves Bühler did an image analysis of the Langtang avalanche and created the satellite images. Jessica Munch helped with the numerical simulation. Perry Bartelt conceived the ideas, built the model, did the simulation, wrote and edited the manuscript.

Competing interests
The authors declare no competing interests.

Additional information
Supplementary information The online version contains supplementary material available at https://doi.org/10.1038/s43247-024-01624-z.

Correspondence and requests for materials should be addressed to Yu Zhuang.

Peer review information *Communications Earth & Environment* thanks Debi Prasanna Kanungo and the other, anonymous, reviewer(s) for their contribution to the peer review of this work. Primary Handling Editor: Alireza Bahadori. A peer review file is available.

Reprints and permissions information is available at http://www.nature.com/reprints

Publisher's note Springer Nature remains neutral with regard to jurisdictional claims in published maps and institutional affiliations.